In-situ N-doped TiO_2/mesoporous g-C_3N_4 nanosheets S-scheme heterojunction derived from supramolecular precursor with enhanced visible-light photocatalytic performance

Changsheng Ban[a,b], Jun Li[a,b],*, Yang Jin[a,b], Longtao Zuo[a,b], Wenqi Xu[a,b]

[a]*School of Chemical Engineering, Sichuan University, Chengdu 610065, China, emails: lijunlab@163.com (J. Li), bcsno1@163.com (C. Ban), jinyangyoung@126.com (Y. Jin), zuolongtao@qq.com (L. Zuo), xuwenqi0401@163.com (W. Xu)*
[b]*Engineering Research Center for Comprehensive Utilization and Cleaning Process of Phosphate Resource, Ministry of Education, Chengdu 610065, China*

ABSTRACT

The N-doped TiO_2/g-C_3N_4 S-scheme heterojunction with holy nanosheet framework has been synthesized by a simple pyrolysis process of amorphous TiO_2 and melamine-cyanaurate complex. During the formation of heterojunction photocatalysts, the interaction of two precursors not only provided in-situ nitrogen doping in TiO_2, but also construct S-scheme charge transfer channel. Also, N-TiO_2/g-C_3N_4 exhibited a porous nanosheet structure due to the co-crystallization of TiO_2 and g-C_3N_4 at 450°C. The enhancement in narrower bandgap and photogenerated charge carrier separation resulted in superior photocatalytic activities with the highest degradation rate of Methylene blue was recorded by MCN/T-50, which was 2.3 and 3.7 times that of bulk g-C_3N_4 and pristine TiO_2. The possible mechanism for the enhanced photocatalytic performance is proposed in this study. The doped S-scheme heterojunction materials prepared from the co-crystallization of precursors in calcination give a broad prospect for the future design of a highly efficient visible-light-driven photocatalyst.

Keywords: N-doped TiO_2; Mesoporous g-C_3N_4; Melamine-cyanaurate complex; S-scheme heterojunction; Degradation

1. Introduction

In recent years, photocatalytic technology has been extensively used for the degradation of organic pollutants, removal of toxic gases and splitting water into hydrogen fuels [1–5]. Among various photocatalysts, TiO_2 is still one of the most promising one due to its environmental friendliness, good chemical stability and high catalytic activity [6]. However, the large bandgap (~3.2 eV) of TiO_2 substantially restricts its response to visible light [7]. To overcome this problem, different modification strategies have been tried, such as shape control [8], element doping [9], construct

heterojunction [10]. Element doping is considered to be an effective method to adjust the energy band structure of TiO_2 [11]. Among various dopants, nitrogen is considered promising owing to its stability, comparable atomic size, and low ionization energy [12]. Although nitrogen-doped TiO_2 (N-TiO_2) exhibits better visible light utilization than pure TiO_2 [13], its photocatalytic performance is still not at a satisfactory stage. Therefore, it is of great importance to modify N-TiO_2.

Nowadays, constructing a step-scheme (S-scheme) heterojunction structure between two semiconductor

* Corresponding author.

materials has proven to be an efficient method to improve the performance of photocatalysts [14–16]. In S-scheme heterojunction, the separation of photogenerated electron–hole pairs is accelerated due to the built-in electric field at the interface. Also, electrons in conduction bands and holes in valance bands with high reduction and oxidation potentials are retained [17]. Among various methods, the all-solid-state reaction under high temperature, which ensures close contact between reactants, is considered to be an effective way for constructing S-scheme heterojunction [18]. Graphitic carbon nitride (g-C_3N_4), a kind of polymer semiconductor, is suitable for preparing heterojunctions with other semiconductors by all-solid-state reaction during thermal polymerization [19]. Also, g-C_3N_4 has advantages of a suitable bandgap (~2.7 eV) to effectively utilize the visible light (λ < 470 nm) and easily modified electronic structure [19]. And precursors of g-C_3N_4 can provide in-situ doped nitrogen during the calcination process [20]. Recently, melamine-cyanaurate complex (MCA), a self-assembled supramolecular, has become an effective precursor of g-C_3N_4. Due to its relatively high thermal stability and ordered hydrogen bond structure, the structural, optical and electronic features of g-C_3N_4 can be optimized [21–24]. Up to now, efforts have been made in fabricating g-C_3N_4/TiO_2 mesoporous heterojunction via self-assembly. For example, Sheng et al. [25] fabricated II-scheme 3D g-C_3N_4/TiO_2 heterojunction by a facile one-step calcination method, which exhibited the effect of adsorption enrichment and photocatalytic activity in the degradation of phenol. Liu et al. [26] prepared well-ordered TiO_2 nanotube arrays decorated with the g-C_3N_4 film via MCA, the close contact between TiO_2 and g-C_3N_4 accelerated the migration of carriers and significantly suppressed the recombination of photogenerated electron–hole carriers, thus exhibiting photoelectrochemical activity. Nevertheless, most of the research are interested in the morphology derived from MCA, few of them focus on the interaction between TiO_2 and g-C_3N_4 during co-crystallization in calcination, which not only influences the morphology of heterojunctions but also greatly effects the type of charge transfer channel.

In this work, the all-solid-phase S-scheme N-TiO_2/g-C_3N_4 heterojunction with holey nanosheet framework is prepared by one-step calcination of supramolecular precursors. It is proposed that the co-crystallization process dopes in-situ nitrogen into the lattice of TiO_2 and makes the contact between two semiconductors more intimate, thus giving more chance to form a built-in electric field. Also, the adsorption capacity is enhanced because gases released by MCA work as porogen. This route provides a promising synthetic route towards the efficient TiO_2/g-C_3N_4 S-scheme heterojunction photocatalysts.

2. Experimental section

2.1. Chemical and materials

All chemicals used in the work were reagent-grade. Dicyandiamide and potassium chloride (KCl) were purchased from Chengdu Chron Chemicals. Titanium tetraisopropanolate (TTIP, 98%) was obtained from Chengdu Best Chemical.

2.2. Catalysis syntheses

2.2.1. Fabrication of mesoporous g-C_3N_4

The mesoporous g-C_3N_4 was synthesized as follows: firstly, dicyandiamide (30 g) was totally dissolved in 60°C deionized water (150 mL). Then it was transferred into a 200 mL Teflon-lined stainless steel autoclave and heated at 160°C for 8 h. The obtained white powder (MCA) was washed with absolute ethanol several times and dried at 60°C for 10 h. Then MCA (2 g) was heated to 450°C in a tube furnace for 3 h with a heating rate of 5°C/min. The final product is denoted as MCN and can be used without further ground. As a comparison, the bulk g-C_3N_4, denoted as BCN, is prepared by calcining melamine (2 g) directly at 550°C in a muffle furnace for 4 h with a heating rate of 5°C/min.

2.2.2. Fabrication of TiO_2 nanoparticles

The anatase TiO_2 was synthesized through controlled hydrolysis of an organometallic precursor followed by calcination in the air: TTIP (4.3 g) was added to ethanol (35 mL) and dissolved by stirring vigorously for 5 min. To achieve controlled hydrolysis, freshly prepared aqueous KCl (15 mL, 0.01 M) was added to the solution in 10 min under vigorous stirring. The stirring was slowed down after 5 min and discontinued after 30 min. The mixture was aging for 15 h to ensure reaction completion. The suspended particles were recovered by centrifuging at 4,000 rpm for 5 min and washed with ethanol 3 times to remove trace reactants. After dried overnight at 60°C, the amorphous powder (0.5 g) was calcined at 450°C for 3 h in a tube furnace with a ramp rate of 5°C/min.

2.2.3. Fabrication of N-TiO_2/g-C_3N_4 heterojunction

A measured quantity of amorphous powder of TiO_2 was grounded finely with MCA (2 g) in an agate mortar. The mixture was transferred in a corundum crucible with a cover for calcinating at 450°C for 3 h with a heating rate of 5°C/min in a tube furnace. The same procedures were repeated by varying the quantity of amorphous powder in the ground mixture that ranges from 30, 40, 50, and 60 mg. The product samples were denoted as MCN/T-30, MCN/T-40, MCN/T-50, MCN/T-60. For comparison, the ground mixture of anatase TiO_2 (50 mg) and MCA (2 g) was calcined under the same procedure, which was denoted as MCN/T-50.

2.3. Characterization

The X-ray powder diffractometer (XRD-6100, Shimadzu) was used for phase analysis of the photocatalysts. The micromorphology of the photocatalysts was investigated using scanning electron microscopy (JSM-7500F, JEOL). Transmission electron microscopy images were obtained by TEM (JEOL JEM 2010 HR). The Brunauer–Emmett–Teller (BET) surface area was examined by Kubo-X1000. The pore-size distribution was measured by exploiting the method of Barrett–Joyner–Halenda. The adsorption volume at P/P_0 = 0.99 was used to determine the pore volume. The thermogravimetric analyzer (Mettler Toledo) was used to study the thermal stability of the sample with heating

temperature under air from 25°C to 800°C, a heating rate of 10°C min^{-1}. The fluorescence spectrophotometer (F700, Hitachi) was used to characterize the photoluminescence (PL) spectrum. The surface chemical state of the material was analyzed using the X-ray photoelectron spectrometer (Axis Supra, Kratos). The electron spin resonance spectrometer (JES-FA200, JEOL Co.) was used for detecting free radicals generated by the photocatalysts under visible light.

2.4. Photocatalytic measurements

The photocatalytic activities of the as-prepared samples were investigated by degradation of Methylene blue (MB) under visible-light irradiation using the Discover-Multichannel photocatalytic reaction system (PCX-50B Beijing Perfectlight Technology Co., Ltd.). 20 mg photocatalyst powder was suspended in 40 mL MB aqueous solution (10 mg/L). The suspension was stirred for 30 min in the dark to establish adsorption–desorption equilibrium. After that, one 5 W LED lamp (white-light source) was used as the visible light source to irradiate the suspensions under vigorous stirring. After irradiation, 4 mL sample solution was collected at a certain time interval, the photocatalysts were removed by the filter, and the remaining solution was analyzed on the UV-Vis spectrometer. The main oxidant species in the degradation of MB was investigated by a free radical capture experiment. The scavengers for hydroxyl radical ($^{\bullet}$OH), photogenerated hole (h$^+$), superoxide radical ($^{\bullet}$O$_2^-$) were isopropanol (IPA), ethylenediaminetetraacetic acid disodium salt (EDTA), and benzoquinone (BQ), respectively. The dosages of all sacrificial agents are 0.01 M.

3. Results and discussion

3.1. Crystallinity and phase analysis

The phase structures of the as-prepared N-TiO$_2$/g-C$_3$N$_4$ samples were investigated by the X-ray diffraction (XRD) analysis, as shown in Fig. 1. MCN shows two distinct peaks at 13.0° and 27.1°. The peak at 13.0° (100) is attributed to the in-plane repeated tris-triazine units while the peak at 27.1° (002) is ascribed to the conjugated aromatic stacking sheets, indicating the formation of g-C$_3$N$_4$ (JCPDS: 87-1526) [27]. Compared to BCN, the (002) peak of MCN shifts to the smaller angel that might be ascribed to uniformly distribute mesopores network resulting in the increased space distance, which is also investigated by some reports of porous g-C$_3$N$_4$ [28]. Meanwhile, the (100) peak of MCN can be barely observed, which indicates that the g-C$_3$N$_4$ nanosheets possess the smaller planar size of the layers [29]. Meanwhile, the intensity of the (002) peak becomes weaker, which may be attributed to the evident size-dependent properties of the g-C$_3$N$_4$ nanosheets [30]. The diffraction peaks at 25.3°, 38.0°, 48.0°, 54.1°, 55.1°, 62.8°, 69.1°, 70.3° and 75.1° could be ascribed to the (101), (004), (200), (105), (211), (204), (116), (220) and (215) planes of the anatase TiO$_2$ (JCPDS: 21-1272) [31]. The peak of the (101) crystal plane becomes more intense with the increment of TiO$_2$ precursor from 30 to 60 mg. Also, the domination of TiO$_2$ nanoparticles with high crystallinity in the samples caused the disappearance of MCN peak characteristics.
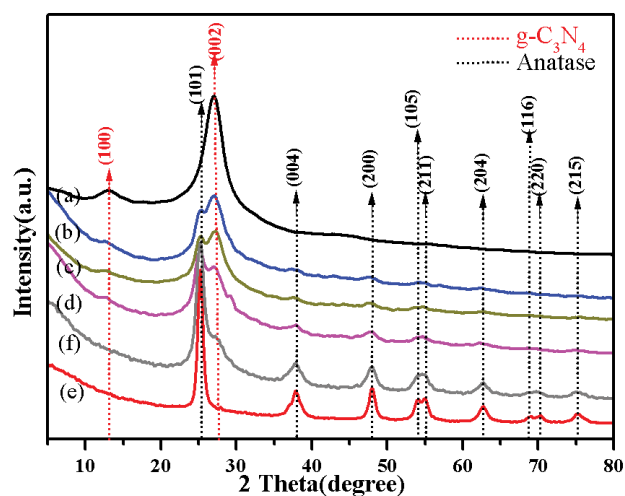

Fig. 1. XRD diffraction pattern of the as-prepared samples (a) MCN, (b) MCN/T-30, (c) MCN/T-40, (d) MCN/T-50, (f) MCN/T-60, and (e) TiO$_2$.

3.2. Morphology

The morphologies of N-TiO$_2$/g-C$_3$N$_4$ heterojunction structures were observed by scanning electron microscopy (SEM), TEM and high-resolution transmission electron microscopy (HR-TEM), as shown in Fig. 2. Fig. 2b shows that TiO$_2$ spherical aggregates are about 200 nm in diameter. As revealed in Fig. 2d, MCN owns a well-defined and interconnected 3D structure with pore sizes between 20–150 nm. However, the SEM images of MCN/T-50 (Fig. 2f) change significantly, TiO$_2$ nanoparticles are conglutinated in the g-C$_3$N$_4$ nanosheets of 3D mesoporous network structure, which reveals the formation of heterojunction between g-C$_3$N$_4$ and TiO$_2$. The morphologies change can be explained as follow: the temperature of amorphous TiO$_2$ dehydration forming anatase TiO$_2$ was above 300°C [32], while the condensation of MCA to generate g-C$_3$N$_4$ was about 400°C [33]. When calcinated by the one-step method, water molecules come from amorphous TiO$_2$ dehydration would decrease the condensation of melamine which reduced the degree of the π-conjugated polymeric network [34]. In the meanwhile, MCA released nitrogen species mainly in the form of NH$_3$, thus mesoporous nanosheets framework of g-C$_3$N$_4$ and interstitial N doping in TiO$_2$ were produced together. Also, the structure of mesoporous g-C$_3$N$_4$, working as a template, efficiently prevented the agglomeration of TiO$_2$ nanoparticles. Thus the diameter of TiO$_2$ aggregates reduced from 200 nm to 40 nm. The smaller nanoparticles of TiO$_2$ and the thinner nanosheets of g-C$_3$N$_4$, corresponding to the intensity changes of XRD peaks in Fig. 1, not only give rise to a more reactive site, but also facilitate photogenerated carrier transfer.

Further, the heterojunction was investigated in the HR-TEM. Image of MCN/T-50 (Fig. 2h), which shows that lattice fringes of 0.327 and 0.35 nm consistent with (002) plane of g-C$_3$N$_4$ and (101) plane of anatase TiO$_2$, respectively [35]. The above results reveal that anchoring and encapsulating of amorphous TiO$_2$ by melamine-cyanuric acid supramolecular preassembly during the calcination
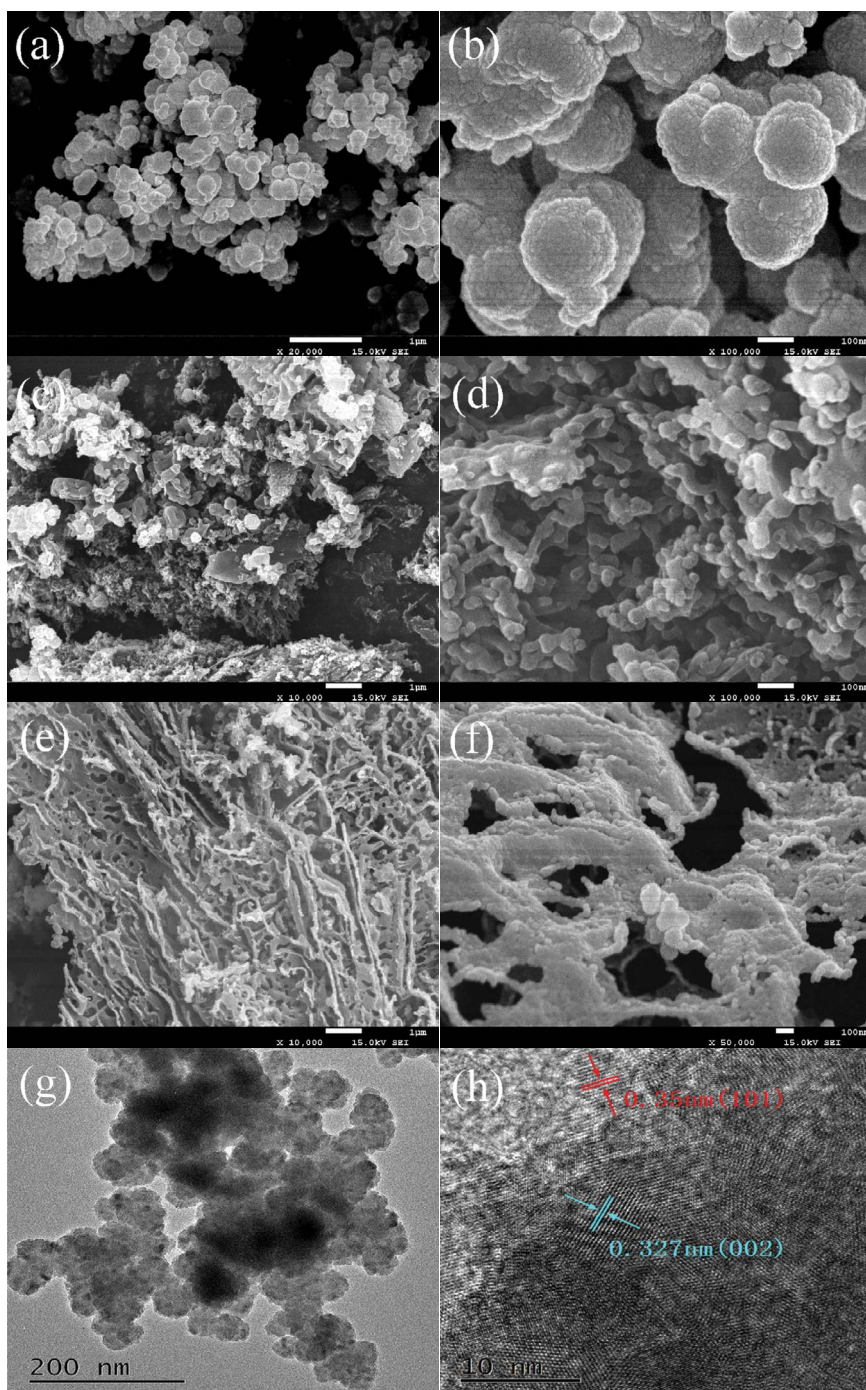
Fig. 2. SEM images of (a, b) TiO$_2$, (c, d) MCN, (e, f) MCN/T-50; TEM and HR-TEM images of (e, f) MCN/T-50.

play a vital role in the inhibition of g-C$_3$N$_4$ aggregation and intimate contact between TiO$_2$ nanoparticles and g-C$_3$N$_4$ nanosheets.

The elemental determination of MCN/T-50 was done through the EDS elemental analysis to confirm the presence of TiO$_2$ and MCN in the samples. As shown in Fig. 3a and b, a well-dispersed and homogeneous TiO$_2$ and MCN and elemental C, N, O and Ti were detected in heterojunctions. The pore size and BET surface area

distributions of N-TiO$_2$/g-C$_3$N$_4$ photocatalysts were studied by N$_2$ adsorption/desorption isotherm, as shown in Fig. 3c. The surface area also plays a very important role in photocatalytic reactivity as a larger specific surface area means more active sites can participate in the photocatalytic reaction [36]. The isotherms of MCN/T heterojunction photocatalysts have hysteresis loops of Type H3 at a high P/P_0 range from 0.8–1.0, indicating the presence of slit-shaped pores resulted from the aggregation of
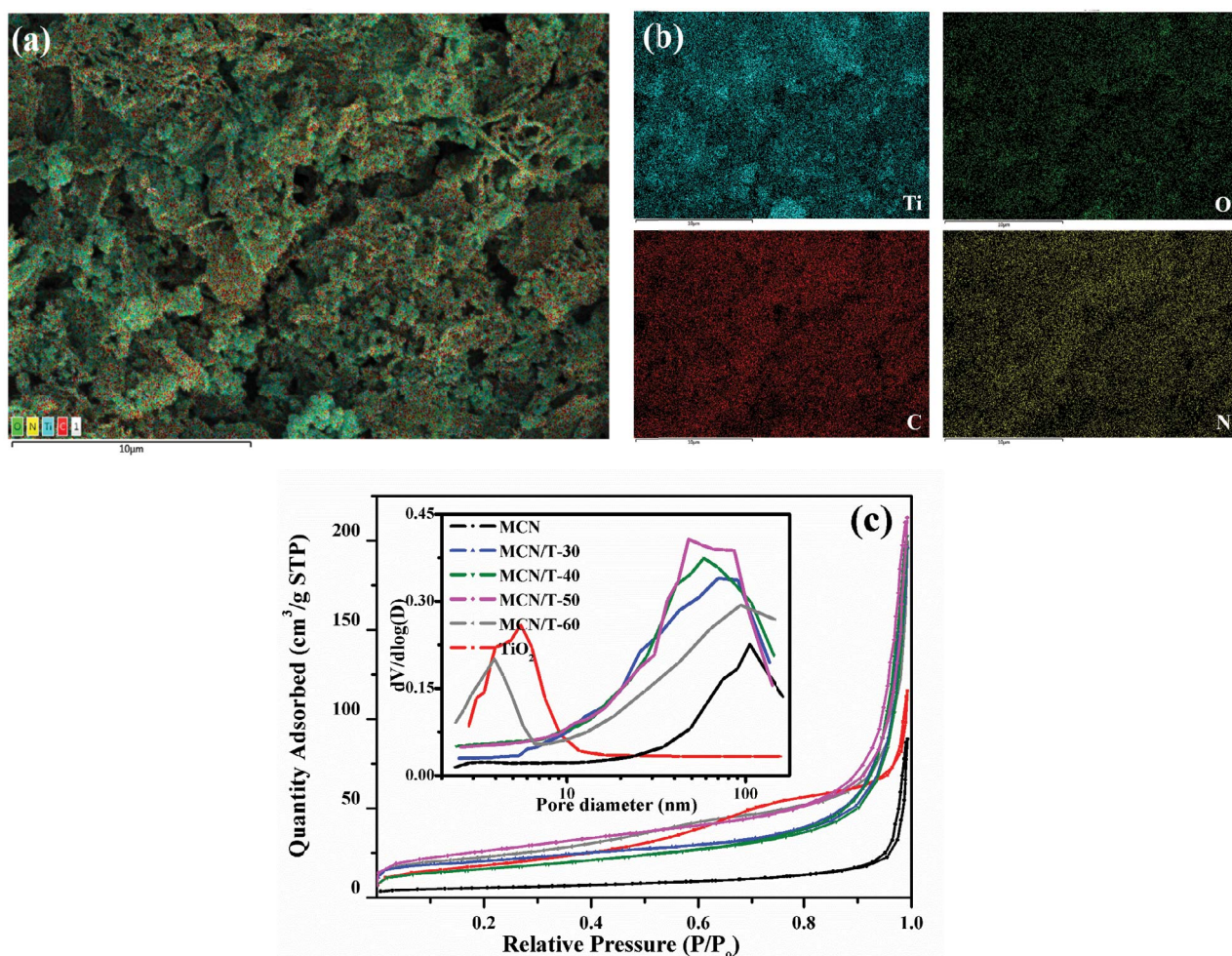
Fig. 3. (a, b) C, N, O and Ti EDS element maps for MCN/T-50 and (c) N_2 adsorption–desorption isotherms and the related pore diameter distribution plots of the as-prepared samples.

plate-like particles [37]. The isotherms show high absorption at a high P/P_0 range (approaching 1.0), implying the formation of large mesopores and macropores, which can be confirmed from SEM results [38]. The specific data is shown in Table 1, the BET surface area (S_{BET}) of MCN/T-50 is as high as 92.6 m^2/g, which is 1.44 and 4.77 times larger than that of TiO_2 (64.2 m^2/g) and MCN (only 19.4 m^2/g), respectively.

3.3. Chemical composition analysis

The chemical compositions and interaction between g-C_3N_4 and TiO_2 in samples MCN/T-50 were analyzed using X-ray photoelectron spectroscopy (XPS) measurement, as shown in Fig. 4. In high-resolution XPS spectra of C 1s, MCN exhibits three deconvolution peaks at 284.6, 287.7 and 288.1 eV, being assigned to C–C, N=C and N–C=N bonds, respectively [39]. In MCN/T-50, N–C=N bonds has smaller percentage than in MCN and the peak of N=C is shifted to 287.6 eV, which is possibly caused by the hybridization effect between g-C_3N_4 and TiO_2 [40].

The HR Ti 2p spectra of pristine TiO_2 can be fitted into two peak positions at 463.7 and 458.0 eV, corresponding to Ti 2p$^{1/2}$ and Ti 2p$^{3/2}$ orbitals, respectively, and the difference in binding energy is 5.7 eV corresponding to the anatase phase. In comparison to more common standard binding energy values (464.4 and 458.7 eV) [41], the positions of Ti 2p$^{1/2}$ and Ti 2p$^{3/2}$ in as-prepared TiO_2 were shifted to lower binding energies, which could be attributed to the relatively low crystallinity of the samples [42]. As for MCN/T-50, part of the electrons generated by the excitation of g-C_3N_4 flow to TiO_2, resulting in an increase in the electron cloud density of Ti 2p, so the binding energy shifts to a higher position [43]. Since the binding energy of the Ti–N bond (456.3 eV) [44] was not observed, it can be inferred that N atoms were inserted into the TiO_2 lattice at the interstitial position instead of the N atom substitution.

In high-resolution XPS spectra of N 1s, MCN/T-50 shows three N 1s peaks at binding energies of 398.3,398.6, and 400.9 eV corresponding to C=N–C, N–$(C)_3$ and C–N–H, while these peaks for MCN are located at 398.4,398.7, and 401.0 eV, respectively [45]. The high binding energies of Ti 2p and lower binding energies of N 1s in the nanocomposite are attributed to the electron migration from the conduction band of TiO_2 to the valence band of g-C_3N_4, which
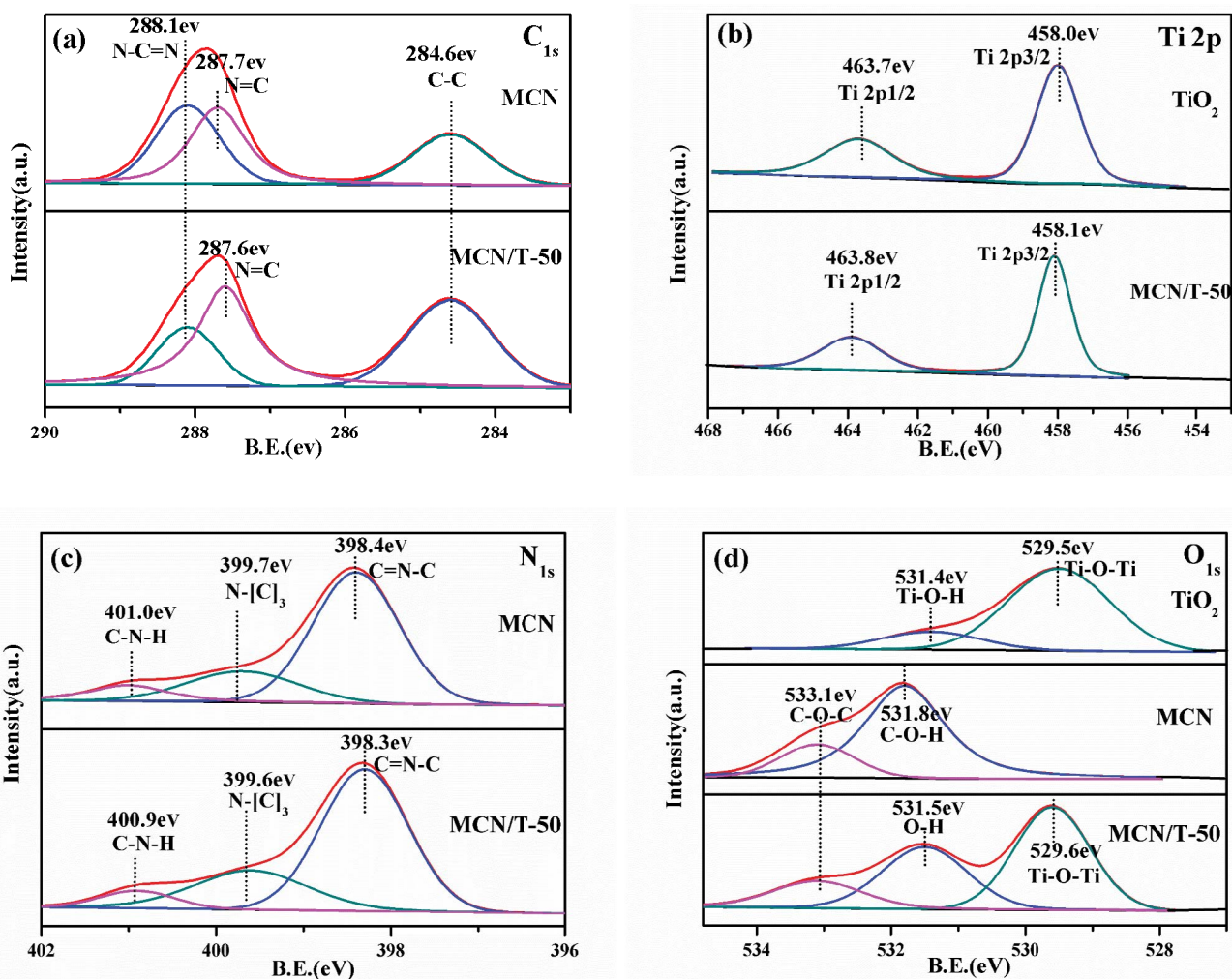
Fig. 4. High-resolution XPS spectra of (a) C 1s, (b) N 1s, (c) O 1s, and (d) Ti 2p.

Table 1
Detailed of textural properties, and weight fraction of the as-prepared samples

Sample	S_{BET} (m^2/g)	Average pore diameter (nm)	Pore volume (cm^3/g)	Weight fraction (%)[a]	
				MCN	TiO$_2$
MCN	19.3	38.5	0.137	100	0
MCN/T-30	57.3	31.5	0.304	78.7	21.3
MCN/T-40	73.8	33.8	0.313	74.0	26.0
MCN/T-50	92.6	36.6	0.330	57.1	42.9
MCN/T-60	80.7	10.9	0.307	37.8	62.2
TiO$_2$	64.2	6.4	0.179	0	100

[a]Data obtained from TGA analysis.

demonstrates the S-scheme charge transfer channel has been successfully constructed [46].

With respect to the O 1s spectrum, two peaks of MCN at 531.5 and 533.1 eV are attributed to Ti–O–H and C–O–H, respectively, indicating that part of oxygen atoms from MCA are still retained into the framework of g-C$_3$N$_4$. It is believed that doped oxygen can capture the photogenerated holes

and inhibit electron–hole recombination [47]. The binding energy of Ti–O–H in TiO$_2$ is 531.4 eV, while C–O–H in MCN is located at 531.8 eV, and the surface hydroxyl of MCN is located at 531.5 eV, which is in the middle of the electron binding energy of the two monomers, which proves that the surface hydroxyls of the two are involved in the calcination process. In the recombination reaction,
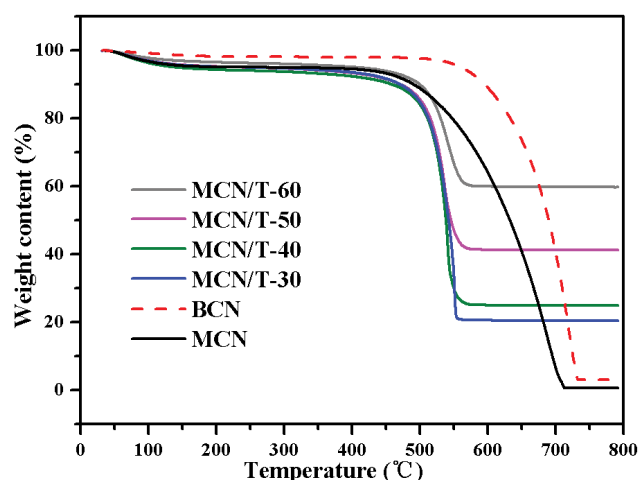
Fig. 5. TGA curves of the as-prepared photocatalysts.

the S-type electron transport channel is possibly established between the role of oxygen on the surface of MCN and TiO$_2$.

3.4. Thermogravimetric analysis

Thermogravimetric analysis (TGA) was conducted to evaluate the thermal stability and component content of as-prepared samples as shown in Fig. 5. It can be seen that BCN exhibits high thermal stability up to 600°C. The highly polymerized tri-s-triazine ring as the major chemical structure in g-C$_3$N$_4$ is responsible for high thermal stability properties. In comparison with BCN, MCN shows relatively poor thermal stability, because released gases and doped oxygen in calcination reduce the degree of polymerization of the tri-s-triazine ring [48]. The decomposition temperature of g-C$_3$N$_4$ in the sample MCN/T-30, MCN/T-40, MCN/T-50 and MCN/T-60 are accelerated at a relatively lower temperature ranging from 450°C to 550°C. The low thermal stability of MCN/T probably results from the disruption and disturbance of the tri-s-triazine chemical structure due to TiO$_2$ interaction and the porous structure.

3.5. Photocatalytic activity in the static system

For investigating the photocatalytic characteristics of different materials, MB gradation experiments were operated under simulated visible light by 5 W LED lamps. A blank experiment without any catalyst was conducted, which revealed that little or no degradation of MB occurred under visible-light illumination as expected. All the as-prepared photocatalysts showed adsorption of MB to different extents in dark conditions. The stronger absorption abilities of MCN/T samples were attributed to its mesoporous structure. As shown in Fig. 6a, the photocatalytic degradation activity of MCN/T enhances a lot compared with MCN and TiO$_2$ under visible light irradiation. With the increasing mass ratio of TiO$_2$, the photocatalytic degradation activity of MCN/T is improved firstly and then decreases. Notably, the highest degradation activity of MCN/T-50 with an apparent rate constant k = 4.591 h^{-1} is shown in Fig. 6b. MCN/T-50 is composed of 57.1% MCN

and 47.9% TiO$_2$ with the highest S$_{BET}$ in the as-prepared samples, as shown in Table 1.

Recycling experiments were carried out on the MB degradation performance of the MCN/T-50 sample for the purpose of evaluating the stability of the mesoporous heterojunctions through its repeated use under visible-light irradiation. As is evident from Fig. 6c, the average MB degradation rate by MCN/T-50 sample for 60 min showed only an insignificant decline from 99.3% to 97.9% through its use in five recycles. The slight reduction is mainly because the sample has some loss when it is centrifuged and dried after each experiment. Fig. 6d shows XRD patterns of MCN/T-50 before and after degradation reaction, where no difference between them demonstrates its outstanding stability as well as repeatability.

3.6. Mechanism of photocatalytic activity enhancement

The optical properties of materials were analyzed by UV-Vis diffuse reflectance spectra (DRS), are displayed in Fig. 7a. TiO$_2$ possesses almost no visible light response (the absorption edge at 387 nm), corresponding to the bandgap of 3.26 eV. It can be seen that MCN photocatalysts exhibit improved light-harvesting ability, with the band absorption edge of 447 nm (bandgap of 2.84 eV), which is originated from the π–π* electron transition upon irradiation. As plotted in Fig. 7b, bulk g-C$_3$N$_4$ possesses a higher visible light absorption capability and a lower bandgap of 2.69 eV. The quantum confinement effect of the building blocks of nanosheets is responsible for the blue-shifted adsorption edge or enlarged bandgap of MCN when compared with BCN [49]. The bandgap of MCN/T-30, MCN/T-40, MCN/T-50, MCN/T-60 is 2.82, 2.81, 2.80, and 2.96 eV, respectively.

The PL spectroscopy analysis was employed to verify the degree of photogenerated electron–hole pairs recombination of the prepared samples. As shown in Fig. 8a, BCN owns the strong characteristic emission peak located at 470 nm, related to the recombination of the photo-induced carriers [50]. The PL intensity of MCN is obviously suppressed compared with BCN, owing to the fast transfer channels provided by the 3D structure of g-C$_3$N$_4$. As to the MCN/T samples, the photoluminescence intensity is gradually weakened with the TiO$_2$ content increasing. The above results indicate that the recombination of photo-induced carriers is efficiently forbad.

To better understand the photocatalytic mechanism of heterojunctions, the band potential of semiconductor photocatalyst can be calculated by the empirical equation [51]:

$$E_{VB} = X - E_e + 0.5\, E_g \tag{1}$$

$$E_{CB} = E_{VB} - E_g \tag{2}$$

where the X is the absolute electronegativity of the semiconductor, and the values are 5.86 and 4.73 eV for TiO$_2$ and g-C$_3$N$_4$, respectively. And E_e, which is the energy of free electrons with the hydrogen scale, is 4.5 eV. The bandgap (E_g) is derived from UV-DRS. Therefore, the calculated valance band (VB) levels for TiO$_2$ and MCN are 2.99 and 1.65 eV, and the estimated conduction band (CB) levels of them are –0.27 and –1.19 eV, respectively. On the one hand,
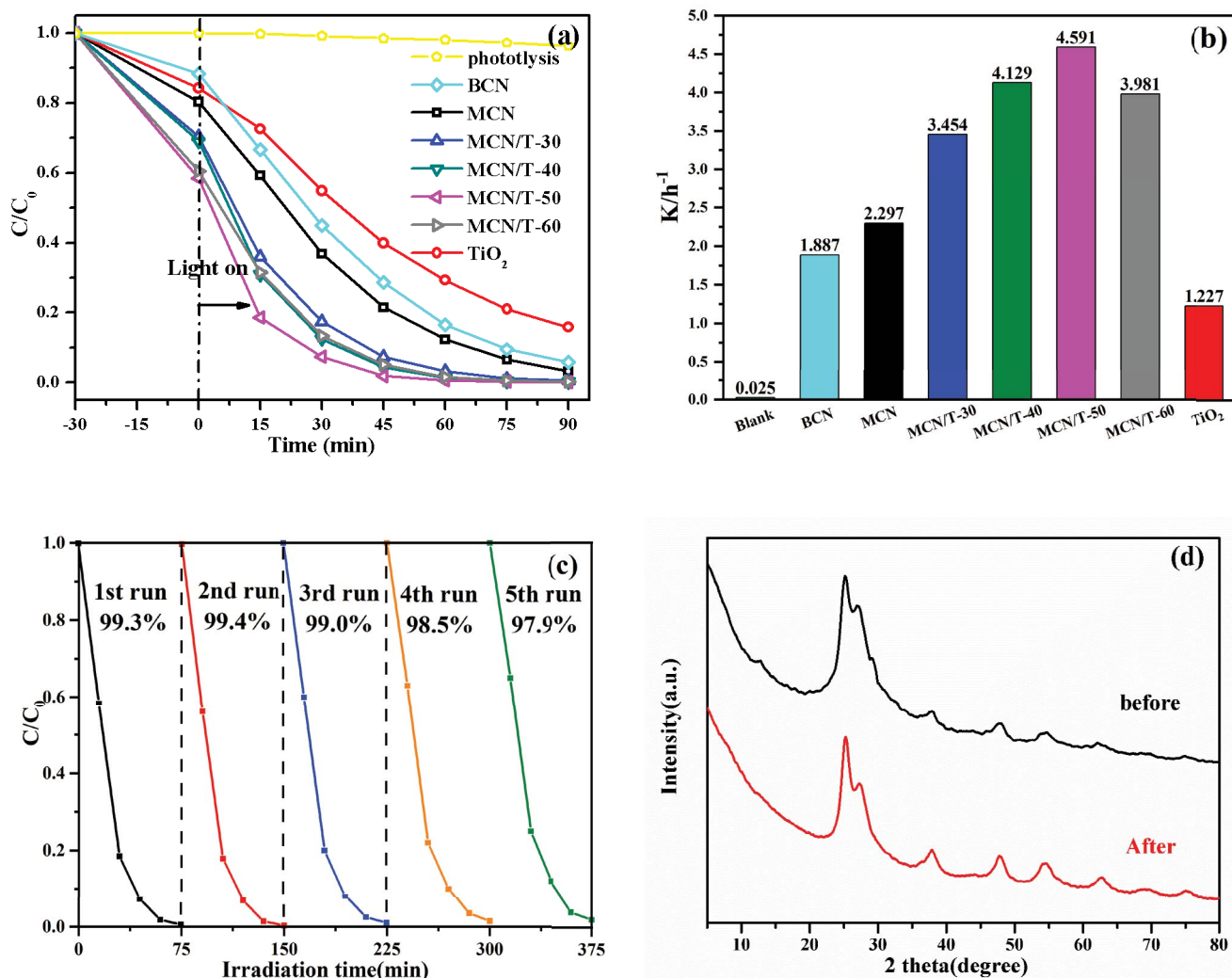
Fig. 6. Photocatalytic activity of the MCN/T and g-C$_3$N$_4$ samples for degradation of MB in aqueous solution: (a) temporal change in MB concentration, (b) the pseudo-first-order rate constants, (c) cycle test curves for the photocatalytic degradation of MB over MCN/T-50 and (d) XRD patterns of MCN/T-50 before and after degradation reaction.

the E_{CB} potentials for both TiO$_2$ and MCN are more negative than the reduction potential of $E°$ (O$_2$/•O$_2^-$), which is –0.046 eV vs. NHE, thus the electrons on the CB of two materials could transfer dissolved oxygen into •O$_2^-$. On the other hand, the potentials of $E°$ (•OH/OH$^-$) and $E°$ (•OH/ H$_2$O) are 1.99 eV vs. NHE and 2.68 eV vs. NHE [34,52], respectively, so only the h$^+$ on the VB of TiO$_2$ can react with OH$^-$ or H$_2$O to generate •OH.

A series of free radical trapping experiments were conducted then. IPA, BQ, and EDTA were employed as the scavengers for •OH, •O$_2^-$ and h$^+$, respectively. As shown in Fig. 8b, the visible light degradation efficiency of anatase TiO$_2$ for MB decreased the most with the addition of IPA, indicating that the most active species of TiO$_2$ is •OH. The degradation efficiency of MCN was reduced the most after BQ is added, indicating that the •O$_2^-$ of the most active species of MCN. For MCN/A-50, the main active species were h$^+$ and •O$_2^-$, while •OH contributed little to the degradation of MB, which meant that MCN/A-50 had a typical type II

charge transport mechanism. The electrons in the CB of MCN flowed to the CB of TiO$_2$ while the h$^+$ in the VB of TiO$_2$ migrated to the VB of MCN, thus the activity of •O$_2^-$ and the production of •OH were significantly decreased. In contrast, all active species produced by MCN/T-50 had a certain contribution to the degradation of MB and the order of their effects are h$^+$ >•O$_2^-$ >•OH.

Based on the above results, the S-scheme heterojunction is proposed to explain the photocatalytic mechanism of MCN/T-50, as shown in Fig. 9. When TiO$_2$ with a higher work function and a lower Fermi level is in close contact with MCN with a smaller work function, electrons will spontaneously migrate from MCN to TiO$_2$ until the Fermi level reaches the same level, therefore, an inner electric field is built [53]. And the energy band of MCN is bent upward due to the loss of electrons, while the band of TiO$_2$ is bent downward. Under simulated visible light, the built-in electric field and bending energy band synergize to accelerate the combination of electrons in the CB of TiO$_2$ and holes in
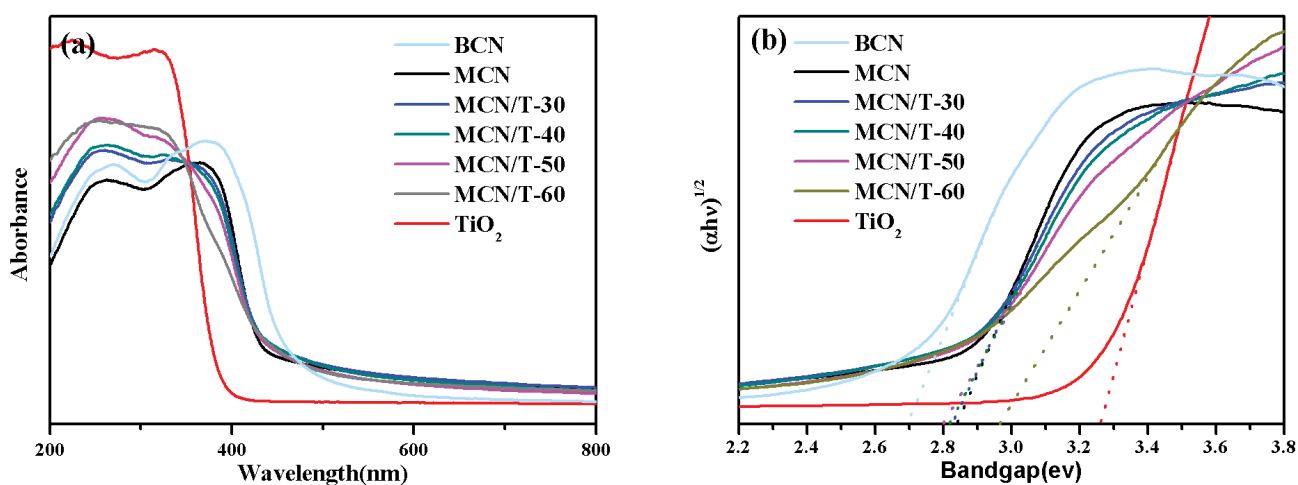
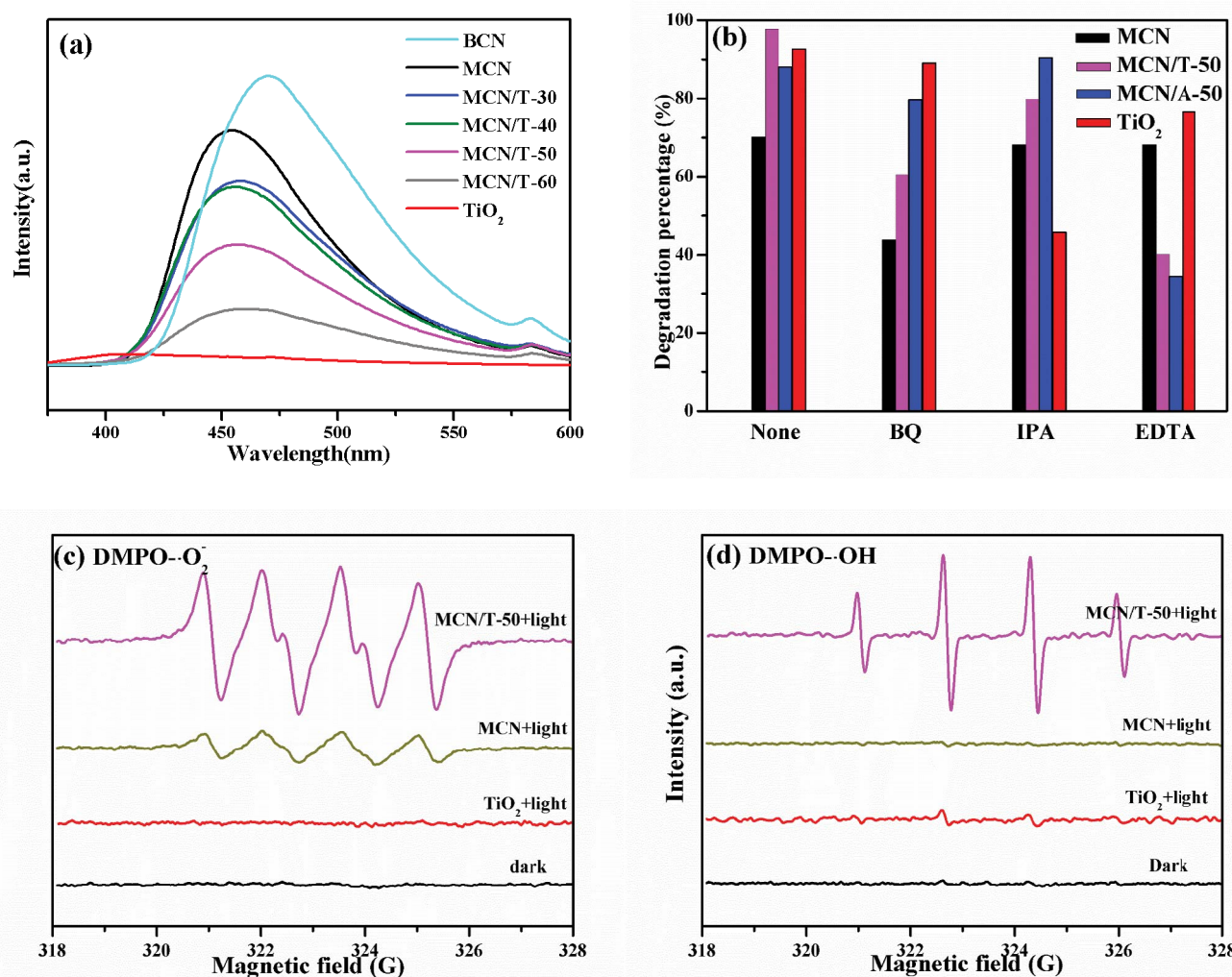Fig. 7. (a) Optical absorption spectroscopy and (b) the estimated band gaps of the as-prepared samples.

Fig. 8. (a) Photoluminescence spectra of the as-prepared samples, (b) photocatalytic activities of TCN for the degradation of MB in the presence of different scavengers under the Xenon lamp irradiation; ESR spectra of the (c) DMPO-$^{•}O_2^-$ and (d) DMPO-$^{•}OH$ adducts recorded with samples under the dark and visible light irradiation.
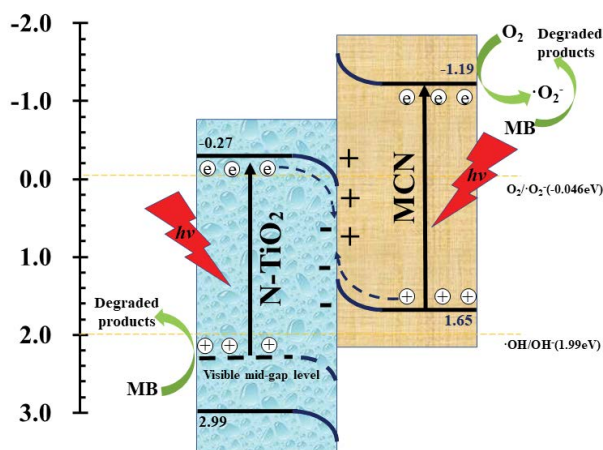
Fig. 9. Proposed bandgap structure and mechanism for photo-degradation of MB.

the VB of MCN, and retain the holes in the VB of TiO_2 and electrons in the CB of MCN, which possess strong redox ability. Also, an intermediate energy level is formed above the VB of TiO_2, which is attributed to the doped N from MCA, thus its visible light response is enhanced. As shown in Fig. 8c and d, both the ESR signals of the trapped $^{\bullet}OH$ and $^{\bullet}O_2^-$ over illuminated MCN/T-50 are much stronger than over MCN and TiO_2, demonstrating the successful doping of nitrogen and construction of S-scheme heterojunction photocatalysts.

4. Conclusion

The N-TiO_2/g-C_3N_4 S-scheme heterojunction photocatalyst with holey nanosheet framework was successfully prepared by direct calcination of amorphous TiO_2 and supramolecular precursor. The in-situ doping of nitrogen in TiO_2 in the composite photocatalyst introduces an intermediate energy level above the VB of TiO_2, which endow it high visible light utilization. The co-crystallization at a relatively high temperature guarantees the intimate contact between g-C_3N_4 and TiO_2, thus the high efficiency of the S-scheme charge transfer channel is constructed. Also, gases released by two precursors in the process of calcination greatly promote the exfoliation of g-C_3N_4 nanosheets, thus large surface areas and more reactive sites are produced. Therefore, the as-prepared S-scheme heterojunction photocatalysts exhibit good photocatalytic performance and cycle stability in degradation of MB, and the highest degradation rate is approximately 2.3 and 3.7 times that of bulk g-C_3N_4 and pristine TiO_2, respectively. The tests of radical scavengers confirmed that $^{\bullet}OH$, $^{\bullet}O_2^-$ and h^+ were all the main reactive species during the photocatalytic process. The synthesis route developed in this study would pave the way for designing elemental doped photocatalytic systems for enhanced organic pollutant degradation.

Conflicts of interests

The authors declare no competing financial interest.

References

[1] J. Fu, J. Yu, C. Jiang, B. Cheng, g-C_3N_4-based heterostructured photocatalysts, Adv. Energy Mater., 8 (2018) 1701503, doi: 10.1002/aenm.201701503.
[2] W. Yu, J. Chen, T. Shang, L. Chen, L. Gu, T. Peng, Direct Z-scheme g-C_3N_4/WO_3 photocatalyst with atomically defined junction for H_2 production, Appl. Catal., B, 219 (2017) 693–704.
[3] K. Kočí, M. Reli, I. Troppov, M. Šihor, J. Kupková, P. Kustrowski, P. Praus, Photocatalytic decomposition of N_2O over TiO_2/g-C_3N_4 photocatalysts heterojunction, Appl. Surf. Sci., 396 (2017) 1685–1695.
[4] J. Low, B. Cheng, J. Yu, Surface modification and enhanced photocatalytic CO_2 reduction performance of TiO_2: a review, Appl. Surf. Sci., 392 (2017) 658–686.
[5] K. Qi, B. Cheng, J. Yu, W. Ho, Review on the improvement of the photocatalytic and antibacterial activities of ZnO, J. Alloys Compd., 727 (2017) 792–820.
[6] V. Kumaravel, S. Mathew, J. Bartlett, S.C. Pillai, Photocatalytic hydrogen production using metal doped TiO_2: a review of recent advances, Appl. Catal., B, 244 (2019) 1021–1064.
[7] S.G. Ullattil, S.B. Narendranath, S.C. Pillai, P. Periyat, Black TiO_2 nanomaterials: a review of recent advances, Chem. Eng. J., 343 (2018) 708–736.
[8] L.P. Domínguez-Jaimes, E.I. Cedillo-González, E. Luévano-Hipólito, J.D. Acuña-Bedoya, J.M. Hernández-López, Degradation of primary nanoplastics by photocatalysis using different anodized TiO_2 structures, J. Hazard. Mater., 413 (2021) 125452, doi: 10.1016/j.jhazmat.2021.125452.
[9] Y. Chen, K. Liu, Fabrication of magnetically recyclable Ce/N co-doped TiO_2/$NiFe_2O_4$/diatomite ternary hybrid: improved photocatalytic efficiency under visible light irradiation, J. Alloys Compd., 868 (2021) 159432, doi: 10.1016/j.jallcom.2016.12.153.
[10] J. Ni, W. Wang, D. Liu, Q. Zhu, J. Jia, J. Tian, Z. Li, X. Wang, Z. Xing, Oxygen vacancy-mediated sandwich-structural TiO_{2-x}/ultrathin g-C_3N_4/TiO_{2-x} direct Z-scheme heterojunction visible-light-driven photocatalyst for efficient removal of high toxic tetracycline antibiotics, J. Hazard. Mater., 408 (2021) 124432, doi: 10.1016/j.jhazmat.2020.124432.
[11] L. Gomathi Devi, R. Kavitha, A review on non-metal ion doped titania for the photocatalytic degradation of organic pollutants under UV/solar light: role of photogenerated charge carrier dynamics in enhancing the activity, Appl. Catal., B, 140 (2013) 559–587.
[12] A. Vesel, R. Zaplotnik, G. Primc, M. Mozetič, A review of strategies for the synthesis of n-doped graphene-like materials, Nanomaterials, 10 (2020) 2286, doi: 10.3390/nano10112286.
[13] M.A. Mohamed, J. Jaafar, M. Zain, L.J. Minggu, M.B. Kassim, Concurrent growth, structural and photocatalytic properties of hybridized C, N co-doped TiO_2 mixed phase over g-C_3N_4 nanostructured, Scr. Mater., 142 (2018) 143–147.
[14] S. Wu, X. Yu, J. Zhang, Y. Zhang, Y. Zhu, M. Zhu, Construction of $BiOCl$/$CuBi_2O_4$ S-scheme heterojunction with oxygen vacancy for enhanced photocatalytic diclofenac degradation and nitric oxide removal, Chem. Eng. J., 411 (2021) 128555, doi: 10.1016/j.cej.2021.128555.
[15] X. Hu, G. Wang, J. Wang, Z. Hu, Y. Su, Step-scheme NiO/BiOI heterojunction photocatalyst for rhodamine photodegradation, Appl. Surf. Sci., 511 (2020) 145499, doi: 10.1016/j.apsusc.2020.145499.
[16] P. Wang, Y. Liu, N. Jiang, R. Jing, S. Li, Q. Zhang, H. Liu, J. Xiu, Z. Li, Y. Liu, Double S-scheme AgBr heterojunction co-modified with g-C_3N_4 and black phosphorus nanosheets greatly improves the photocatalytic activity and stability, J. Mol. Liq., 329 (2021) 115540, doi: 10.1016/j.molliq.2021.115540.
[17] Q. Xu, L. Zhang, B. Cheng, J. Fan, J. Yu, S-scheme heterojunction photocatalyst, Chem, 6 (2020) 1543–1559.

[18] M. Ismael, A review and recent advances in solar-to-hydrogen energy conversion based on photocatalytic water splitting over doped-TiO$_2$ nanoparticles, Sol Energy, 211 (2020) 522–546.

[19] M. Ismael, A review on graphitic carbon nitride (g-C$_3$N$_4$) based nanocomposites: synthesis, categories, and their application in photocatalysis, J. Alloys Compd., 846 (2020) 156446, doi: 10.1016/j.jallcom.2020.156446.

[20] J. Li, B. Li, Q. Li, J. Yang, The effect of N-doped form on visible light photoactivity of Z-scheme g-C$_3$N$_4$/TiO$_2$ photocatalyst, Appl. Surf. Sci., 466 (2019) 268–273.

[21] Z. Tong, D. Yang, Y. Sun, Y. Nan, Z. Jiang, Tubular g-C$_3$N$_4$ isotype heterojunction: enhanced visible-light photocatalytic activity through cooperative manipulation of oriented electron and hole transfer, Small, 12 (2016) 4093–4101.

[22] S. Guo, Z. Deng, M. Li, B. Jiang, C. Tian, Q. Pan, H. Fu, Phosphorus-doped carbon nitride tubes with a layered micro-nanostructure for enhanced visible-light photocatalytic hydrogen evolution, Angew. Chem. Int. Ed. Engl., 55 (2016) 1830–1834.

[23] K. Li, X. Xie, W.D. Zhang, Porous graphitic carbon nitride derived from melamine-ammonium oxalate stacking sheets with excellent photocatalytic hydrogen evolution activity, ChemCatChem, 8 (2016) 2128–2135.

[24] S. Li, Y. Peng, C. Hu, B. Chen, Self-assembled synthesis of benzene-ring-grafted g-C$_3$N$_4$ nanotubes for enhanced photocatalytic H$_2$ evolution, Appl. Catal., B, 279 (2020) 119401, doi: 10.1016/j.apcatb.2020.119401.

[25] Y. Sheng, Z. Wei, H. Miao, W. Yao, H. Li, Y. Zhu, Enhanced organic pollutant photodegradation via adsorption/photocatalysis synergy using a 3D g-C$_3$N$_4$/TiO$_2$ free-separation photocatalyst, Chem. Eng. J., 370 (2019) 287–294.

[26] C. Liu, F. Wang, J. Zhang, K. Wang, Y. Qiu, Q. Liang, Z. Chen, Efficient photoelectrochemical water splitting by g-C$_3$N$_4$/TiO$_2$ nanotube array heterostructures, Nano-Micro Lett., 10 (2018) 37, doi: 10.1007/s40820-018-0192-6.

[27] M.A. Mohamed, M. Zain, L.J. Minggu, M.B. Kassim, J. Jaafar, N.A.S. Amin, Y.H. Ng, Revealing the role of kapok fibre as bio-template for In-situ construction of C-doped g-C$_3$N$_4$@C, N co-doped TiO$_2$ core-shell heterojunction photocatalyst and its photocatalytic hydrogen production performance, Appl. Surf. Sci., 476 (2019) 205–220.

[28] S. Wu, S. Wen, X. Xu, G. Huang, Y. Cui, J. Li, A. Qu, Facile synthesis of porous graphene-like carbon nitride nanosheets with high surface area and enhanced photocatalytic activity via one-step catalyst-free solution self-polymerization, Appl. Surf. Sci., 436 (2018) 424–432.

[29] Q. Han, B. Wang, Y. Zhao, C. Hu, L. Qu, A graphitic-C$_3$N$_4$ "seaweed" architecture for enhanced hydrogen evolution, Angew. Chem. Int. Ed. Engl., 54 (2015) 11433–11437.

[30] Z. Mo, H. Xu, Z. Chen, X. She, Y. Song, J. Wu, P. Yan, L. Xu, Y. Lei, S. Yuan, H. Li, Self-assembled synthesis of defect-engineered graphitic carbon nitride nanotubes for efficient conversion of solar energy, Appl. Catal., B, 225 (2018) 154–161.

[31] S. Tan, Z. Xing, J. Zhang, Z. Li, X. Wu, J. Cui, J. Kuang, Q. Zhu, W. Zhou, Ti^{3+}-TiO$_2$/g-C$_3$N$_4$ mesostructured nanosheets heterojunctions as efficient visible-light-driven photocatalysts, J. Catal., 357 (2018) 90–99.

[32] M. Zhang, Z. Jin, J. Zhang, X. Guo, J. Yang, W. Li, X. Wang, Z. Zhang, Effect of annealing temperature on morphology, structure and photocatalytic behavior of nanotubed H$_2$Ti$_2$O$_4$(OH)$_2$, J. Mol. Catal. A: Chem., 217 (2004) 203–210.

[33] Q. Liu, X. Wang, Q. Yang, Z. Zhang, X. Fang, Mesoporous g-C$_3$N$_4$ nanosheets prepared by calcining a novel supramolecular precursor for high-efficiency photocatalytic hydrogen evolution, Appl. Surf. Sci., 450 (2018) 46–56.

[34] Z. Wang, W. Guan, Y. Sun, F. Dong, Y. Zhou, W.K. Ho, Water-assisted production of honeycomb-like g-C$_3$N$_4$ with ultralong carrier lifetime and outstanding photocatalytic activity, Nanoscale, 7 (2015) 2471–2479.

[35] L. Shi, L. Liang, F. Wang, M. Liu, K. Chen, K. Sun, N. Zhang, J. Sun, Higher Yield urea-derived polymeric graphitic carbon nitride with mesoporous structure and superior visible-light-responsive activity, ACS Sustainable Chem. Eng., 3 (2015) 3412–3419.

[36] R. Yang, J. Cai, K. Lv, X. Wu, W. Wang, Z. Xu, M. Li, Q. Li, W. Xu, Fabrication of TiO$_2$ hollow microspheres assembly from nanosheets (TiO$_2$-HMSs-NSs) with enhanced photoelectric conversion efficiency in DSSCs and photocatalytic activity, Appl. Catal., B, 210 (2017) 184–193.

[37] R. Hao, G. Wang, H. Tang, L. Sun, C. Xu, D. Han, Template-free preparation of macro/mesoporous g-C$_3$N$_4$/TiO$_2$ heterojunction photocatalysts with enhanced visible light photocatalytic activity, Appl. Catal., B, 187 (2016) 47–58.

[38] J. Yu, S. Wang, J. Low, W. Xiao, Enhanced photocatalytic performance of direct Z-scheme g-C$_3$N$_4$-TiO$_2$ photocatalysts for the decomposition of formaldehyde in air, Phys. Chem. Chem. Phys., 15 (2013) 16883–16890.

[39] J. Li, M. Zhang, X. Li, Q. Li, J. Yang, Effect of the calcination temperature on the visible light photocatalytic activity of direct contact Z-scheme g-C$_3$N$_4$-TiO$_2$ heterojunction, Appl. Catal., B, 212 (2017) 106–114.

[40] L. Ma, G. Wang, C. Jiang, H. Bao, Q. Xu, Synthesis of core-shell TiO$_2$@g-C$_3$N$_4$ hollow microspheres for efficient photocatalytic degradation of rhodamine B under visible light, Appl. Surf. Sci., 430 (2018) 263–272.

[41] J. Schneider, M. Matsuoka, M. Takeuchi, J. Zhang, Y. Horiuchi, M. Anpo, D.W. Bahnemann, Understanding TiO$_2$ photocatalysis: mechanisms and materials, Chem. Rev., 114 (2014) 9919–9986.

[42] R. Ren, Z. Wen, S. Cui, Y. Hou, X. Guo, J. Chen, Controllable synthesis and tunable photocatalytic properties of Ti^{3+}-doped TiO$_2$, Sci. Rep., 5 (2015) 10714, doi: 10.1038/srep10714.

[43] Y.T. Lin, C.H. Weng, Y.H. Lin, C.C. Shiesh, F.Y. Chen, Effect of C content and calcination temperature on the photocatalytic activity of C-doped TiO$_2$ catalyst, Sep. Purif. Technol., 116 (2013) 114–123.

[44] C. Gebauer, J. Fischer, M. Wassner, Novel N, C doped Ti(IV)-oxides as Pt-free catalysts for the O$_2$ reduction reaction, Electrochim. Acta, 146 (2014) 335–345.

[45] W. Wang, J. Fang, S. Shao, M. Lai, C. Lu, Compact and uniform TiO$_2$@g-C$_3$N$_4$ core-shell quantum heterojunction for photocatalytic degradation of tetracycline antibiotics, Appl. Catal., B, 217 (2017) 57–64.

[46] D. Liang, Y. Huang, F. Wu, J. Luo, X. Yi, J. Wang, X. Qiu, In situ synthesis of g-C$_3$N$_4$/TiO$_2$ with {001} and {101} facets co-exposed for water remediation, Appl. Surf. Sci., 487 (2019) 322–334.

[47] J. Ma, D. Jin, Y. Li, D. Xiao, G. Jiao, Q. Liu, Y. Guo, L. Xiao, X. Chen, X. Li, J. Zhou, R. Sun, Photocatalytic conversion of biomass-based monosaccharides to lactic acid by ultrathin porous oxygen doped carbon nitride, Appl. Catal., B, 283 (2021) 119520, doi: 10.1016/j.apcatb.2020.119520.

[48] A. Wang, C. Wang, L. Fu, W. Wong-Ng, Y. Lan, Recent advances of graphitic carbon nitride-based structures and applications in catalyst, sensing, imaging, and LEDs, Nano-Micro Lett., 9 (2017) 47, doi: 10.1007/s40820-017-0148-2.

[49] Y. Duan, X. Li, K. Lv, L. Zhao, Y. Liu, Flower-like g-C$_3$N$_4$ assembly from holy nanosheets with nitrogen vacancies for efficient NO abatement, Appl. Surf. Sci., 492 (2019) 166–176.

[50] Y. Wang, W. Yang, X. Chen, J. Wang, Y. Zhu, Photocatalytic activity enhancement of core-shell structure g-C$_3$N$_4$@TiO$_2$ via controlled ultrathin g-C$_3$N$_4$ layer, Appl. Catal., B, 220 (2018) 337–347.

[51] Y. Shang, X. Chen, W. Liu, P. Tan, H. Chen, L. Wu, C. Ma, X. Xiong, J. Pan, Photocorrosion inhibition and high-efficiency photoactivity of porous g-C$_3$N$_4$/Ag$_2$CrO$_4$ composites by simple microemulsion-assisted co-precipitation method, Appl. Catal., B, 204 (2017) 78–88.

[52] X.J. Wang, W.Y. Yang, F.T. Li, Y.B. Xue, R.H. Liu, Y.J. Hao, In-situ microwave-assisted synthesis of porous N-TiO$_2$/g-C$_3$N$_4$ heterojunctions with enhanced visible-light photocatalytic properties, Ind. Eng. Chem. Res., 52 (2013) 17140–17150.

[53] J. Wang, G. Wang, B. Cheng, Sulfur-doped g-C$_3$N$_4$/TiO$_2$ S-scheme heterojunction photocatalyst for Congo Red photodegradation, Chin. J. Catal., 42 (2021) 56–68.